Article:

de Boer, GN, Hewson, RW, Thompson, HM et al. (2014) Two-scale EHL: three-dimensional topography in tilted-pad bearings. Tribology International, 79. 111 - 125. ISSN: 0301-679X

https://doi.org/10.1016/j.triboint.2014.05.019

Tribology International 79 (2014) 111–125

Contents lists available at ScienceDirect

Tribology International

journal homepage: www.elsevier.com/locate/triboint

Two-scale EHL: Three-dimensional topography in tilted-pad bearings

G.N. de Boer [a,*], R.W. Hewson [b], H.M. Thompson [a], L. Gao [b], V.V. Toropov [c]

[a] School of Mechanical Engineering, University of Leeds, Leeds, LS2 9JT, UK
[b] Department of Aeronautics, Imperial College London, London, SW7 2AZ, UK
[c] School of Engineering and Materials Science, Queen Mary University of London, London, E1 4NS, UK

ARTICLE INFO

Article history:
Received 25 January 2014
Received in revised form
13 May 2014
Accepted 16 May 2014
Available online 6 June 2014

Keywords:
EHL
Topography
Multiscale method
Tilted-pad bearings

ABSTRACT

Derived from the Heterogeneous Multiscale Methods (HMM), a two-scale method is developed for the analysis of Elastohydrodynamic Lubrication (EHL) and micro-EHL in tilted-pad bearings with three-dimensional topography. A relationship linking the pressure gradient to mass flow rate is derived and represented in the bearing domain through homogenisation of near-periodic simulations describing the Fluid Structure Interaction (FSI) of topographical features. For the parameters investigated the influence of compressibility and piezoviscosity was found to be more significant than that of non-Newtonian (shear-thinning) behaviour on textured bearing performance. As the size of topography increased two-scale solutions demonstrated that at constant load the coefficient of friction increased and the minimum film thickness decreased over a range of pad lengths and tilt angles.

1. Introduction

The Reynolds equation [1] is well established as an accurate means of describing fluid flow in the Elastohydrodynamic Lubrication (EHL) of smooth surface geometries [2]. More recently the focus of lubrication engineers has been directed toward analysis of surface topography and the influence that this has on bearing load capacity and friction coefficients [3]. The potential of topographical features to improve bearing performance has increased the importance of surface roughness and texturing within bearing design [4]. A number of authors have sought solutions to the Reynolds equation which fully resolve lubrication flow at both the scale of topography and that of the bearing contact region [5–8]. As topographical features become more important flow analyses based on solutions of the Stokes or Navier–Stokes equations have been shown to be more accurate than those based on the traditional Reynolds equation [9].

Studies which compare solutions to Reynolds, Stokes and Navier–Stokes equations for textured surfaces have been conducted by a number of researchers [10–15]. For more details see Gao and Hewson [16]. Significant differences in load capacity between Reynolds and Stokes solutions were found in the presence of topographical features. The inclusion of inertial effects via the generalised Reynolds equation [17] or Navier–Stokes equations illustrated the influence of inertia on load capacity and the consequent benefit of using Computational Fluid Dynamics (CFD) to model the fluid film flow. CFD has also been used on smooth geometries to enable the modelling of a range of phenomena which occur in EHL such as thermal transport, rheology, cavitation [18], wall slip [19] and structural models [20].

Both deterministic (where the surface topographical features are fully described and resolved over the global domain) and homogenisation (where the flow about surface topographical features are solved independently and the results are applied to the global domain) models have been used by researchers to analyse bearings with surface texturing. Although CFD has the potential to comprehensively describe lubrication phenomena most research in this field to date remains focused on the use of the Reynolds equation, whether that is by deterministic [21–24] or homogenisation [11,25–28] models. Few deterministic models have been developed which employ the Navier–Stokes equations [11,29] because of the large separation in scales between each local feature and the entire domain. The grid resolution required to model such a difference is beyond most computational facilities, making a homogenisation based approach more feasible.

Patir and Cheng [30] introduced the average flow model where the Reynolds equation is modified with flow factors that allow the scale of topography and that of the domain to be treated separately. These flow factors were calculated from simulations describing the local surface texture with periodic boundary conditions which are subsequently coupled into a global-scale

---

Abbreviations: ALE, Arbitrary Lagrangian-Eulerian; CFD, Computational Fluid Dynamics; CV, Cross Validation; DoE, Design of Experiments; EHL, Elastohydrodynamic Lubrication; FE, Finite Element; FSI, Fluid Structure Interaction; HMM, Heterogeneous Multiscale Methods; MLS, Moving Least Squares; OLHC, Optimum Latin Hypercube; PTFE, Polytetrafluoroethylene; RMSE, Root Mean Squared Error; RSM, Response Surface Methodology

[*] Corresponding author. Tel.: +44 7411 050709.
E-mail address: mn07gndb@leeds.ac.uk (G.N. de Boer).

http://dx.doi.org/10.1016/j.triboint.2014.05.019

Nomenclature

A, ΔA	Area, area deformation (m^2)
$C_1 - C_{10}$	MLS constants
D_0, D_1	Dowson–Higginson compressibility
E, E'	Young's modulus, equivalent modulus (Pa)
$\boldsymbol{F}$	Force per unit volume (N/m^3)
g	Film gap (μm)
h	Undeformed film thickness (μm)
$\boldsymbol{K}, \boldsymbol{K}_G$	Stiffness matrix, global stiffness matrix (μm/MPa)
k_1	Local stiffness (μm/MPa)
k	Number of folds
L	Cell length (μm)
L_p	Pad length (mm)
p, Δp	Pressure, pressure jump (MPa)
p_r	Viscous reference pressure (GPa)
p^*	Load-per-unit-area (N/mm^2)
q	Mass flow rate (kg/s)
r	Micro-EHL effect on minimum film thickness (%)
s	Small scale film thickness (μm)
Δs	Deformation of small scale film thickness (μm)
s_{min}	Small scale minimum film thickness (μm)
t, t'	Pad thickness, equivalent thickness (mm)
U	Wall velocity (m/s)
$\boldsymbol{u}$	Fluid velocity (m/s)
u, v, w	Fluid velocity components (m/s)
V	Volume (m^3)
W	Load capacity (kN)
x, y, z	Spatial coordinates (m)
Z	Piezoviscous index
α	Topography amplitude (μm)
$\dot{\gamma}$	Shear rate (1/s)
δ	Deformation (μm)
δ_t	Topography function (μm)
η, η_0	Viscosity, ambient viscosity (Pa s)
η_p	Piezoviscosity (Pa s)
η_r	Roelands reference viscosity (Pa s)
μ	Coefficient of friction
ν	Poisson's ratio
ρ, ρ_0	Density, ambient density (kg/m^3)
σ	Stress (N/m^2)
τ, τ_0	Shear stress, Eyring stress (N/mm^2)
φ	Tilt angle (°)

simulation. Using this average flow model Sahlin et al. [26] developed a method of homogenisation for hydrodynamic bearings with periodic roughness, the flow factors were calculated from homogenised results of the compressible Reynolds equation. This concept was then extended by Sahlin et al. [27] to a mixed lubrication regime with prescribed sinusoidal roughness. Still using the Reynolds equation to describe the small scale fluid flow, a contact mechanics model was used to determine both elastic and plastic asperity deformation. Solid–solid contact was implemented to derive the bearing surface and as such Fluid Structure Interaction (FSI) was not considered at either scale.

Studies have been conducted where Navier–Stokes equations are used to describe the small scale problem. de Kraker et al. [31,32] applied the incompressible Navier–Stokes equations to describe small scale fluid flow and an averaged Reynolds equation (similar to that of Patir and Cheng [30]) was implemented at the large scale. Flow factors were introduced to account for the small scale simulations but micro-EHL effects were not considered. A similar model was developed for discrete cell gravure roll coating by Hewson et al. [33]. A relationship was derived linking homogenised results of Stokes flow simulations at the small scale to a pressure gradient – mass flow rate relationship at the large scale. The linearity of Stokes flow allowed for simple integration of the small scale simulations into the large scale simulation.

Based on the Heterogeneous Multiscale Method (HMM) developed by E and Engquist [34], a framework for the analysis of micro-EHL in two-dimensions was outlined by Gao and Hewson [16]. Both local and global EHL effects were described. The incompressible Navier–Stokes equations were used to define fluid flow at the small scale. Results of near-periodic small scale simulations were homogenised and applied to the global solution via a pressure gradient – mass flow rate relationship. Periodicity was vital to the coupling mechanism, allowing small scale simulations to be treated as a point at the large scale. The resulting relationship binding these two scales was shown to be non-linear due to deformation of the bearing surface and small scale flow effects. Interpolation was used at the large scale to inspect between previously obtained small scale results. These results were collected via a full factorial Design of Experiments (DoE). Deformation at both scales was treated through the separation of the stiffness matrix into local and non-local influences. Results of smooth surface simulations at the small scale were presented and compared well with lubrication theory when applied to a tilted-pad bearing problem. Results including topography demonstrated the influence of micro-EHL and the robustness of this method in capturing these effects.

In this study the multiscale framework outlined by Gao and Hewson [16] is extended to three-dimensional small scale simulations and more representative lubricant behaviour is considered. The two-scale method derived is valid where the bearing has no cross-flow or side-leakage. However, additional comments are made as to how the general solution can be achieved. The steady-state, isothermal, laminar and compressible Navier–Stokes equations govern fluid flow at the small scale, where piezoviscosity and non-Newtonian (shear-thinning) behaviour are also modelled. A method for the homogenisation of small scale simulations in three-dimensions is introduced. This data is similarly coupled to the large scale via a pressure gradient – mass flow rate relationship. The small scale data is represented by a Moving Least Squares (MLS) approximation, a metamodel describing this relationship is built and validated using k-fold Cross Validation (CV) in a method similar to that used by Loweth et al. [35] and Narayanan et al. [36]. This method employs an Optimum Latin Hypercube (OLHC) to populate the DoE used for small scale simulations, in order to span the entire design space as effectively as possible with the fewest number of designs [37,38]. Numerical simulations of this multiscale approach are presented for a range of topography amplitudes and compared to lubrication theory over a range of operating conditions and degrees of freedom.

2. Theory

2.1. Heterogeneous multiscale method (HMM)

The HMM is a general modelling technique that can be employed where there is a distinct separation in scales ([34]). As a starting point a solver is chosen for a known large scale model, in which some terms are explicitly unknown. The HMM replaces these unknown quantities with results of numerical simulations at the small scale. The key to the application of HMM proposed by Gao and Hewson [16] was how the two scales were coupled and the application of near-periodicity at the small scale. By using the same rationale a similar, though more general, formulation is described here. Small scale results describe the pressure gradient – mass flow rate relationship and through homogenisation, the large scale subsequently applies this to a global pressure distribution and conservation of mass. This approach is limited because only small scale inertial effects can be included. By neglecting large scale inertia the resulting simulation is consistent with the assumptions which define lubrication theory. Large scale variables influence the homogenised relationship through interpolation of the small scale solutions. In this method a metamodel is used in place of the small scale data as a route to interpolation.

2.2. *Large scale simulation*

The large scale simulation describes EHL in the global bearing domain. In a manner similar to that of conventional EHL analyses, hydrodynamic pressure in the lubricant is coupled with elastic deformation of the bearing surface.

2.2.1. *Fluid flow model*

One-dimensional flow is considered at the large scale in this study. This is governed by equations for the pressure gradient and mass conservation

$$\frac{dp}{dx}=f(p,q,g) \tag{1}$$

$$\frac{dq}{dx}=0 \tag{2}$$

The pressure gradient (dp/dx) is a homogenised function of the pressure (p), mass flow rate per unit width (q) and film gap (g). The three parameters on the right hand side of Eq. (1) are the only large scale parameters which influence small scale flow. This data is obtained from the small scale simulations, the details of which can be found in the following section. Dirichlet boundary conditions apply to Eqs. (1) and (2) such that pressure at the global inlet (p_a) and outlet (p_b) is zero (ambient pressure):

$$p_a=p_b=0 \tag{3}$$

The one-dimensional large scale problem could be extended to two-dimensions to account for cross-flow or side-leakage by deriving a similar expression to that given by Eq. (1), whereby the relationship between the flow rate in both the x and y directions can be expressed as functions of the pressure gradients in these directions, the pressure, and local large scale geometry. Conservation of mass in the x and y directions can then be applied to solve the two-dimensional problem.

2.2.2. *Elastic deformation*

Elastic deformation of the bearing surface is determined in a similar manner to classic EHL analyses. See Cameron [39] for more details. Deformation is found via a matrix operation, where the influence of pressure on displacement decreases with the distance from the point at which it is applied. The total deformation influence matrix ($\boldsymbol{K}$), or deformation coefficient matrix, is calculated using elasticity theory [40]. The relationship describing how pressure (load per unit area) relates to surface deformation is given by the following equation:

$$\delta=\boldsymbol{K}p \tag{4}$$

2.2.3. *Separation of the deformation matrix*

Eq. (4) can be rewritten such that total deformation is the sum of local and non-local influences

$$\delta=k_1\boldsymbol{I}p+\boldsymbol{K}_Gp \tag{5}$$

In Eq. (5), k_1 is the local large scale stiffness comprising of only diagonal matrix terms which is subsequently modelled at the small scale. The term $k_1\boldsymbol{I}p$ accounts for local deformation and $\boldsymbol{K}_Gp$ non-local deformation. Where $\boldsymbol{K}_G$ is the global deformation influence matrix, this can be solved for given the relationship with the total deformation matrix in Eq. (6)

$$\boldsymbol{K}_G=\boldsymbol{K}-k_1\boldsymbol{I} \tag{6}$$

Separating deformation of the pad into these two terms highlights how deformation at local and global scales can be treated independently. By implementing this mechanism local, micro-EHL and global EHL effects are described.

2.2.4. *Pressure–deformation coupling*

By separating the deformation influence matrix into the large scale problem described the influence of local deformation (characterised by the local stiffness (k_1)) on the the pressure gradient – mass flow rate relationship is included through Eq. (1), which is determined at the small scale and subsequently applied to the large scale simulation. The film gap (g) becomes the sum of the undeformed film thickness (h) and non-local deformation

$$g=h+\boldsymbol{K}_Gp \tag{7}$$

Eqs. (1), (2) and (7) are coupled and solved iteratively until convergence in the pressure distribution is reached. Due to the presence of topography at the small-scale Eq. (1) will also model micro-flow and structural effects which are not described by the large scale mechanics, as described in the following section.

2.3. *Small scale simulations*

The small scale simulations are defined by steady-state, isothermal, compressible, laminar flow as described by Navier–Stokes equations and those which govern elastic deformation of the small scale features. Coupling is achieved through an Arbitrary Lagrangian–Eulerian (ALE) approach in a Finite Element (FE) simulation.

2.3.1. *Spring column representation*

The small scale EHL model is based on the fluid flow due to topography and the local stiffness properties. Deformation at the small scale uses an equivalent thickness (t') of the solid domain to ensure that the resulting deformation due to fluid pressure is equal to the column deformation achieved from the local stiffness (k_1) at the large scale.

$$t'=k_1E' \tag{8}$$

The equivalent elastic modulus (E') is derived to represent the mechanical properties of the large scale problem to a fully constrained column of bearing material in three-dimensions at the small scale [40].

$$E'=\frac{(1-\nu)E}{(1+\nu)(1-2\nu)} \tag{9}$$

where E and ν are Young's modulus and Poisson's ratio of the bearing material respectively. Eq. (9) is not valid for incompressible materials ($\nu=0.5$) since t' will tend to infinity, invalidating the spring column approach. By applying an equivalent thickness to the problem the small scale FSI is accurately described whilst maintaining the required stiffness properties at the large scale. It is important to note that this approach is only valid where the size of the equivalent thickness is an order of magnitude greater than the

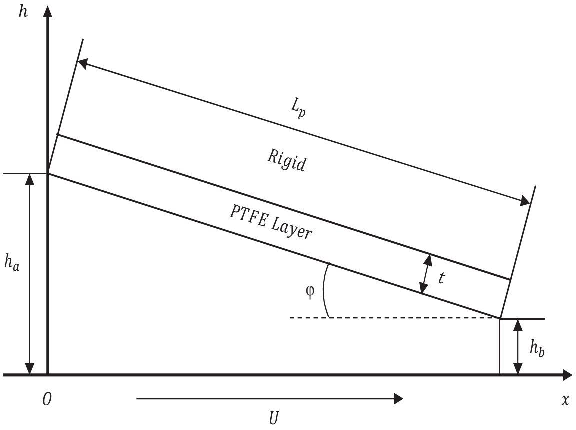

Fig. 1. Large scale bearing geometry.

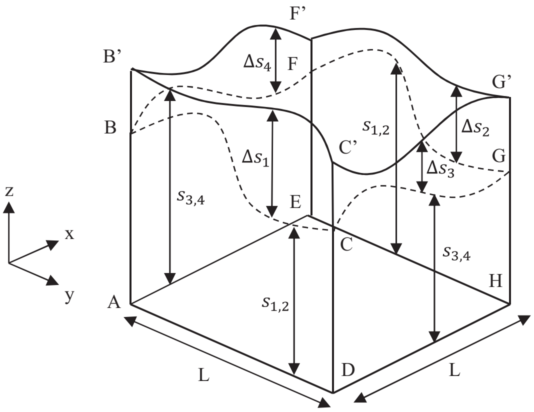

Fig. 3. Deformed small scale fluid domain.

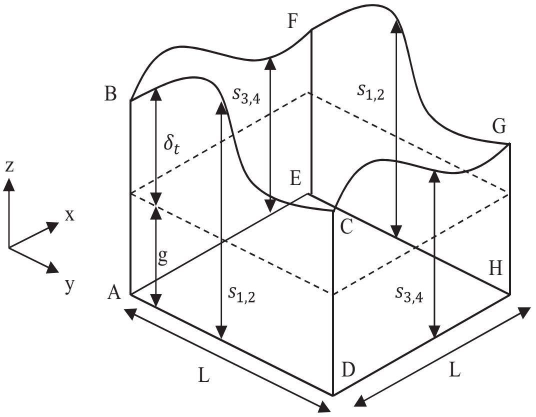

Fig. 2. Small scale fluid domain.

size and deformation of the topographical feature. Because discretisation at the large scale determines local stiffness, ensuring this condition raises some challenges, as will be discussed below.

2.3.2. *Fluid domain*

Fig. 2 illustrates the small scale fluid domain used in this study. The domain is described by the undeformed film gap (g) and the cell size (L) in both the x and y dimensions respectively. For the purpose of simplicity the cell size in both dimensions are equal, however this is not a requirement for the approach. The cell film thickness (s) is the sum of film gap (g) and the periodic function describing topography (δ_t).

$$s = g + \delta_t \tag{10}$$

Periodicity must be maintained in the cell film thickness (pre-deformation) at the boundaries in order to satisfy the multiscale theory. Therefore the function describing topography must also be periodic. Eq. (11) has been chosen for the purpose of this study however more complex topography could be generated by using Fourier analysis to combine a number of periodic functions. α is the topography amplitude where a value of $\alpha = 0$ corresponds to a smooth surface, the solution for which can be directly described by Reynolds equation

$$\delta_t = \frac{\alpha}{4}\left[\sin\left(2\pi\frac{x}{L} - \pi\right) + \sin\left(2\pi\frac{y}{L} - \pi\right) + 2\right] \tag{11}$$

Parameterisation of topography is possible using this two-scale method, the parameters describing δ_t would become additional variables in the pressure gradient – mass flow rate relationship (Eq. (1)). Due to the increased computational cost associated with this, a single topography has therefore been chosen for this study. The different topography amplitudes investigated are represented through multiple metamodels.

2.3.3. *Fluid flow model*

The small scale flow is considered steady, laminar, compressible and isothermal as described by Navier–Stokes equations in the following form [41]:

$$\nabla \cdot (\rho \boldsymbol{u}) = 0 \tag{12}$$

$$\rho(\boldsymbol{u} \cdot \nabla)\boldsymbol{u} = \nabla \cdot \left[-p\boldsymbol{I} + \eta(\nabla\boldsymbol{u} + (\nabla\boldsymbol{u})^T) - \frac{2}{3}\eta(\nabla \cdot \boldsymbol{u})\boldsymbol{I}\right] \tag{13}$$

where ρ denotes the fluid density, η is the fluid viscosity, p is the fluid pressure, $\boldsymbol{u}$ is the velocity vector and $\boldsymbol{I}$ is the unit tensor.

2.3.4. *Fluid properties*

Compressibility is modelled via the Dowson–Higginson (D–H) equation where fluid density is barotropic [42]. ρ_0 is the ambient density, and D_0, D_1 are constants.

$$\rho = \rho_0 \frac{D_0 + D_1 p}{D_0 + p} \tag{14}$$

Viscosity is both piezoviscous and non-Newtonian (shear-thinning). The piezoviscous response is governed by Eq. (15) as defined by Roelands [43]. η_p is the piezoviscous viscosity, η_0 is the viscosity at ambient conditions, η_r is the Roelands reference viscosity, p_r is the Roelands reference pressure, and Z the pressure–viscosity index [44].

$$\eta_p = \eta_r \exp\left(\ln\left(\frac{\eta_0}{\eta_r}\right)\left(1 + \frac{p}{p_r}\right)^Z\right) \tag{15}$$

Shear-thinning behaviour is modelled using the Ree-Eyring model as originally developed by Johnson and Tevaarwerk [45] and further refined by Bair et al. [46], where τ_0 is the Eyring stress and $\dot{\gamma}$ is the shear rate, Eq. (16) is derived.

$$\eta = \frac{\tau_0}{\dot{\gamma}} \sinh^{-1}\left(\frac{\eta_p \dot{\gamma}}{\tau_0}\right) \tag{16}$$

2.3.5. *Fluid boundary conditions*

In reference to Fig. 2 the fluid flow boundary conditions are described. The lower surface *ADHE* is a moving wall with velocity U in the x-coordinate direction. *BCGF* is a no-slip boundary which forms the fluid/solid interface. The remaining faces form two sets of near-periodic (scaled to account for deformation and compressibility) boundaries, *ABCD*/*EFGH* and *ABFE*/*DCGH*. The boundaries which are normal to the direction of motion of the moving wall

(*ABCD*/*EFGH*) experience a jump in pressure, generating a pressure gradient in x over the domain. The other set (*ABFE*/*DCGH*) remains fully periodic with pressure as no gradient is required in this direction for the large scale solution. If the large scale model requires such gradients then these can be generated by another jump condition imposed on these boundaries.

The pressure jump condition is modelled by Eq. (17) where the pressure profile is shifted by a constant Δp. Subscripts 1 and 2 denote downstream and upstream boundaries respectively.

$$p_2 = p_1 + \Delta p \tag{17}$$

Deformation of the upper surface creates challenges when implementing a boundary condition for velocity because the resulting outward facing area (A) of each pair face is no longer equal, as portrayed in Fig. 3.

Mass flow rate must be equal at the boundaries in order to satisfy mass conservation and the HMM analysis. This enables us to derive a near-periodic boundary condition for velocity Eq. (18) and corresponding Eqs. (19) and (20) for density and area ratios.

$$\boldsymbol{u}_2 = \boldsymbol{u}_1 \cdot \frac{\rho_1}{\rho_2} \cdot \frac{A_1}{A_2} \tag{18}$$

$$\frac{\rho_1}{\rho_2} = \frac{(D_0 + D_1 p_1)(D_0 + p_1 + \Delta p)}{(D_0 + p_1)(D_0 + D_1(p_1 + \Delta p))} \tag{19}$$

$$\frac{A_1}{A_2} = \frac{1 + (\Delta A_1 / A_0)}{1 + (\Delta A_2 / A_0)} \tag{20}$$

Eq. (19) accounts for compressibility at the boundaries. Eq. (20) describes how the ratio of areas relates to the strain in area over the boundary. A_0 is the boundary outward facing area pre-deformation and ΔA is the area deformation of the boundary. This boundary condition is consistent with the HMM, where near-periodicity is maintained over a small scale feature. As the scale separation increases this becomes an increasingly valid assumption. If the length of the small scale feature tends toward zero and the small scale feature vanishes the problem can be solved analytically, and the lubrication equation is obtained.

2.3.6. *Solid domain*

The solid is located above the fluid domain as illustrated by Fig. 4. FSI occurs at the interface connecting the two domains. The thickness (t') is derived as previously outlined from the material and stiffness properties required at the large scale. Topography (δ_t) is removed from the solid column. The size and subsequent deformation of topography must be an order of magnitude smaller than the solid column thickness such that the local topography dependent stress field is not affected.

2.3.7. *Solid deformation model*

Structural mechanics is considered at the small scale using a conventional three-dimensional FE analysis in order to represent the local stiffness (k_1) required at the large scale. The force balance is characterised by Eq. (21) where the solid material is assumed homogeneous, isotropic and linearly elastic [47].

$$-\nabla \cdot \sigma = \boldsymbol{F} V \tag{21}$$

where σ is the normal stress tensor, $\boldsymbol{F}$ is the vector of load per unit volume, and V is the volume.

2.3.8. *Solid boundary conditions*

With reference to Fig. 4 the small scale solid boundary conditions are described. The upper boundary *PQSR* is fully constrained. The sides of the spring column *BPQC*, *BPRF*, *FRSG* and *CQSG* are constrained normal to the surface. The fluid/solid interface *BCGF* is loaded by the pressure p generated from the fluid flow simulations, i.e. the stress normal to the boundary is equal to the pressure.

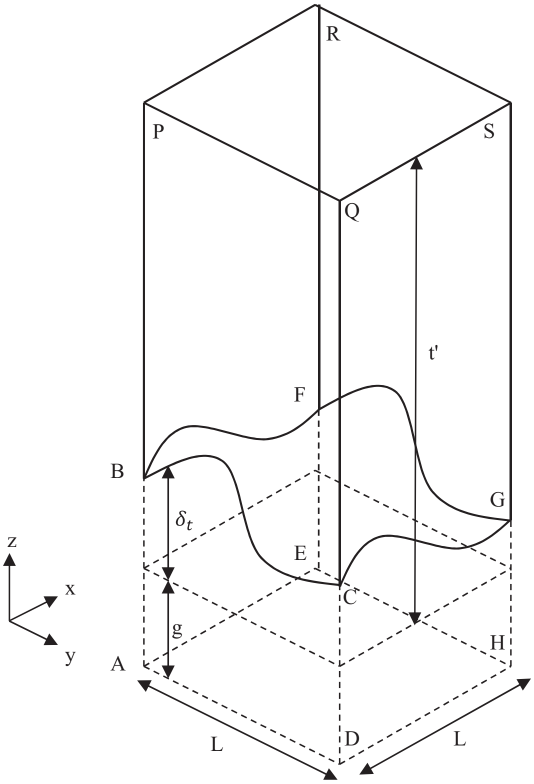

Fig. 4. Small scale solid domain.

2.4. *Homogenisation*

Given a pressure constraint (placed directly in the centre of *ADHE* of Fig. 2, denoted by p_0) and the initial gap (g, which includes the undeformed film thickness plus deformation of non-diagonal terms of the stiffness matrix, excluding the diagonal terms), the solution fields for pressure and velocity can be obtained by solving for the small scale model. The homogenised pressure gradient (dp/dx) over a unit cell is calculated using Eq. (22).

$$\frac{dp}{dx} = \frac{\Delta p}{L} \tag{22}$$

The mass flow rate per unit width (q) at the large scale is determined from the mass flow rate which characterises the small scale flow and the magnitude of the extra dimension considered at this scale. Eq. (23) is calculated on the deformed boundary *AB′C′D* of Fig. 3.

$$q = \frac{1}{L} \int_0^{s+\Delta s} \int_0^L \rho u dy dz \tag{23}$$

where Δs is the deformation of the fluid domain thickness. The pressure constraint (p_0), pressure gradient (dp/dx), initial gap (g), and the mass flow rate per unit width (q) are required for interpolation of the small scale results for use in a large scale simulation.

As pressure is not linearly distributed in the small scale domain due to effects which occur in the presence of topography as well as that due to deformation, compressibility, piezoviscosity, etc., an average cell pressure(p^*) is derived which describes the load per unit area in the large scale simulation and from which the load capacity of the bearing is determined.

$$p^* = \frac{1}{L^2}\int_0^L \int_0^L p \ dx \ dy \tag{24}$$

This pressure is used to determine the deformation at the large scale. The shear force per unit area (τ) is calculated from Eq. (25) at the small scale, this is equivalent to shear stress in the large scale model. The integration of Eqs. (24) and (25) is over the moving wall boundary *ADHE* of Fig. 2.

$$\tau = \frac{1}{L^2}\int_0^L \int_0^L \eta \frac{du}{dz} dx \, dy \tag{25}$$

The small scale minimum film thickness (s_{min}) can be reported using Eq. (26). This film thickness is representative of the micro-EHL effect and is thus a measure of the deformation of the small scale features. Eq. (26) is performed on the deformed fluid/solid interface $B'C'G'F'$.

$$s_{min} = \min_{x,y}(s + \Delta s) \tag{26}$$

The role of additional flow phenomenon (viscosity, density) cannot be shown at the large scale because they vary significantly in the small scale solutions, meaning that homogenisation does not reflect the true magnitude of the variable in the small scale domain.

2.5. Lubrication theory

When considering fluid flow the smooth surface case (where the size of the topography is zero, $\alpha = 0$) can be compared with Reynolds equation to provide a benchmark for the multiscale approach. This is because without topography inertial forces will become negligible and the small scale problem can be accurately described by the lubrication approximation. Eq. (27) is the corresponding Reynolds equation in one-dimension using the separation of the stiffness matrix.

$$\frac{dp}{dx} = \frac{12\eta}{\rho(g+k_1p)^3}\left(\frac{\rho U}{2}(g+k_1p) - q\right) \tag{27}$$

2.6. Response surface methodology (RSM)

Representation of the small scale data at the large scale is achieved through the use of a Moving Least Squares (MLS) approximation. The approximation describes the small scale solutions over the entire design space. The design space encompasses the complete range of values required by the large scale solver. RSM refers to the process of building, validating and implementing the approximation based on the previously obtained experiments, this is also known as surrogate or metamodelling [48]. Creating a model of this nature requires a Design of Experiments (DoE) which ensures the most efficient spread of simulations in the design space. An Optimum Latin Hypercube (OLHC) is used here to cover as much of the design space with as few designs as possible [37]. Eq. (1) is replaced by Eq. (28) where the tilde notation represents known values corresponding to small scale simulations of the evaluated function and θ is a metamodel tuning parameter. Similar representations are defined for the load per unit area (p^*), shear force per unit area (τ), and small scale minimum film thickness (s_{min}).

$$\frac{dp}{dx} \simeq \tilde{f}\left(\tilde{p}, \tilde{g}, \tilde{q}, \tilde{\frac{dp}{dx}}, p, g, q, \theta\right) \tag{28}$$

2.6.1. Moving least squares (MLS) approximation

MLS is derived from conventional weighted least squares model building where the weights do not remain constant but are functions of the normalised Euclidian distances from sampling points to the point where the metamodel is evaluated. The weight associated with a particular sampling point decays as an evaluation point moves away from the sampling point. It is not possible to obtain an analytical form of the MLS function representing the metamodel but its evaluation is computationally inexpensive and therefore used in this work. Eqs. (29)–(32) illustrate polynomial basis functions used to model the multiscale relationships for the pressure gradient, load per unit area, shear force per unit area, and small scale minimum film thickness respectively. Each of these is based upon the corresponding lubrication theory models but inclusive of extra constants which are determined through the MLS operation. These constants ($C_1 - C_{10}$) are functions of the position within the design space at which the metamodel is being assessed. The dimensions of C_3 are MPa/mm, C_5 and C_8 are N/mm^2, C_{10} is μm, and the remaining constants are dimensionless.

$$\frac{dp}{dx} = \frac{12\eta_0}{\rho_0(g+k_1p)^3}\left(\frac{C_1\rho_0 U}{2}(g+k_1p) - C_2 q\right) + C_3 - 1 \tag{29}$$

$$p^* = C_4 p + C_5 - 1 \tag{30}$$

$$\tau = \frac{-6\eta_0}{\rho_0(g+k_1p)^2}\left(\frac{2C_6\rho_0 U}{3}(g+k_1p) - C_7 q\right) + C_8 - 1 \tag{31}$$

$$s_{min} = C_9(g+k_1p) + C_{10} - 1 \tag{32}$$

Deviations from lubrication theory introduced by the small scale model are captured by these constants. In the incompressible, isoviscous, smooth surface case the set of constants will be unity throughout the design space as the computational results are the same as lubrication theory.

MLS metamodels can be tuned to the DoE data by varying the closeness of fit parameter θ. Changing θ controls the rate at which the weight decays with distance from a sampling point or in another perspective the sphere of influence surrounding an evaluation point beyond which a sample point will have no effect on the resulting metamodel approximation. This parameter allows MLS approximations to efficiently deal with numerical noise, where the user has choice over how 'close' or 'loose' the fit is [49]. Several strategies have been derived in order to automatically predict the closeness of fit parameter for a given data set [50]. Following from the work of Loweth et al. [35] θ is determined using the k-fold Cross Validation (CV) method.

2.6.2. k-Fold cross validation (CV)

In k-fold CV a random set of size k is removed from the DoE and the MLS approximation is built from the remaining sample points (building set) using a given closeness of fit parameter (θ). The approximation is then compared against the known function value at the removed locations (validation set) by calculating the Root Mean Squared Error (RMSE).

$$RMSE = \sqrt{\frac{1}{k}\sum_{i=1}^{i=k}(f_i - \tilde{f}_i)^2} \tag{33}$$

In Eq. (33) k is the number of validation points, $\tilde{f}_i$ belongs to the set of known function evaluations and f_i to the set of corresponding MLS approximations. This process of error checking is repeated over many k-sized folds of the validation set as to include all points in both the building and validation phases. An average of the RMSE is then used to provide the error for the approximation at the current closeness of fit parameter (θ). A range of θ values is specified and the above process is carried out across this range. The smallest average RMSE predicted gives the value of the closeness of fit which produces the most accurate MLS approximation for the data provided. The average RMSE versus closeness of fit parameter response is subject to a significant amount of numerical noise making the search for a minimum RMSE difficult. Practical experience [35] suggests that the following must all be specified in order to reduce this noise: the number of repeat folds (1000 is chosen to limit numerical cost), the size of each fold used (~30% of the DoE size), the method of randomisation by which folds are chosen, and the range of the closeness of fit parameter chosen for investigation (this can vary between zero (least squares regression) and any value until over-fitting occurs [51], the range of 0–100 was found to be suitable in this case).

3. Numerical method

3.1. Geometry and materials

Fig. 1 illustrates the linear-converging tilted-pad bearing which is analysed in this study at the large scale. The convergent geometry will minimise cavitation in the outlet region as pressure will always remain above the ambient value, although this may not necessarily hold at the small scale where micro-cavitation could conceivably occur. The pad length (L_p) is representative of the contact region for the bearing. The thickness of the deformable polytetrafluoroethylene (PTFE) layer (t) is large enough to incorporate deformation from the resulting simulation. The rigid backing to the pad is undeformable. A minimum undeformed film thickness for the tilted-pad bearing (h_b) at the outlet is adjusted at a constant tilt angle (φ) such that the undeformed film thickness distribution (h) is given by the following equation:

$$h = h_b + (L_p \cos \varphi - x) \tan \varphi \tag{34}$$

Topography is defined at the small scale but may be parameterised at the large scale, as outlined earlier. These topographical features are assumed to be evenly distributed across the length of the pad on the PTFE layer, this layer is assumed to remain stationary throughout. The lower surface of the bearing contact moves with speed U in the x-coordinate direction. The lubricant modelled is compressible, piezoviscous and non-Newtonian (shear-thinning) and the solid is linearly elastic as outlined earlier. Details for the constants related to these fluid and solid properties plus those used as operating conditions are listed in Table 1.

3.2. Stiffness properties

In this study only elastic deformation of the pad is modelled and bending is not considered. The stiffness matrix ($\boldsymbol{K}$) is calculated using the method described by Rodkiewicz and Yang [52]. The FE method is used to model solid deformation of the pad. From the principle of virtual work stiffness properties for the pad are derived. The pad is discretised and unit loads applied to each of the pad face elements in turn. The resulting deformation distributions become a row in the total deformation matrix. As these distributions are superimposed they provide the pad deformation due to pressure acting on all elements. This can be scaled directly to account for any load within the elastic limit of the material. As such the value of the diagonal terms of the matrix which govern the large scale local stiffness is affected by the size of elements chosen to represent the bearing surface. This leads to a potential breakdown of the multiscale theory required at the small scale. In order for the spring column approach to remain valid, the magnitude of deformation at the small scale must be at least an order of magnitude smaller than the equivalent thickness derived from the local stiffness properties. If the discretisation is too large the resulting thickness becomes too small for this assumption to hold. The stiffness at the small scale is set to a value which will always provide a large enough thickness, the local stiffness (k_1). The resulting small scale simulations provide a solution at this stiffness. Because deformation is linear the result can be scaled directly to match the required large scale local stiffness, resulting in Eq. (7). In order to model the required load per unit area derived from small scale simulations Eq. (7) is replaced by Eq. (35).

Table 1
Parameters values and ranges.

Parameter	Value/Range	Unit
D_0, D_1	0.59×10^9, 1.34	–
E	0.5	GPa
k_1	0.4667	μm/MPa
L	10	μm
L_p	[20, 25]	mm
p_r	0.196	GPa
U	1	m/s
W	75, 100	kN
Z	0.4486	–
α	[0, 7.5]	μm
η_0	1	Pa.s
η_r	6.31×10^{-5}	Pa.s
ν	0.4	–
ρ_0	870	kg/m^3
τ_0	5	N/mm^2
φ	[0.05, 0.06]	deg

$$g = h + \boldsymbol{K}_G p^* \tag{35}$$

In this study the local stiffness is constant and thus the same small scale data can be used for any large scale definition of the stiffness matrix. In this sense the formulation outlined here is more general than the method specified by Gao and Hewson [16].

3.3. Solution procedure

The first stage of the solution procedure is to determine suitable ranges for the gap, pressure and pressure gradient which will produce useful flow rates for the multiscale approach. Approximate limits were found by running equivalent simulations with Reynolds equation (Eq. (27)) replacing the homogenised small scale simulations, the resulting limits are tabulated in Table 2. The DoE was specified using an OLHC code [37] and the small scale simulations run using the FE solver COMSOL Multiphysics (USA). k-fold CV was subsequently performed on the resulting data sets to find the closeness of fit parameters needed for the MLS approximations, ready for large scale implementation.

For a given large scale undeformed geometry, the solution procedure begins with an initial guess for the pressure distribution. This is chosen as the corresponding smooth surface solution to the Reynolds equation. The film gap is then updated according to Eq. (35) to include non-diagonal deformation terms. The pressure was then solved based on this updated geometry and the pressure gradient – mass flow rate relationship (Eq. (1)), which is inclusive of the local elastic deformation obtained for the small scale simulations. The actual representation of this is governed by the MLS approximation (Eq. (29)) derived after the small data is acquired. This process is repeated until convergence of the pressure field, the tolerance chosen for this was 10^{-3}. For each iteration deformation is relaxed by a factor of 0.5 due to instabilities in the numerical solution method.

Table 2
Ranges applied to the DoE used for the small scale simulations.

Parameter	Range	Unit
$\frac{dp}{dx}$	[−40, 10]	MPa/mm
p	[0, 10]	MPa
g	[5, 50]	μm

The solution for Eqs. (1) and (2) is achieved via a shooting method for the mass flow rate to satisfy the boundary conditions for pressure. In this method the MATLAB (The MathsWorks Inc., USA) initial value solver ode45 has been used to perform 4th/5th order Runge–Kutta integration to solve for the pressure field. The mass flow rate is adjusted after each iteration dependening on whether the error in the pressure boundary condition at outlet is either under or over predicted. This function returns the pressure, pressure gradient, load per unit area, shear force per unit area and mass flow rate for the current gap.

In order to undertake physically meaningful comparisons between different operating conditions and degrees of freedom an operating load capacity was specified for each simulation. This load was obtained by adjusting the minimum undeformed film thickness (h_b) using a bisector approach. Once this load is reached the minimum film thickness (g_b) and coefficient of friction (μ) are recorded where the actual bearing load (W) and μ are given by Eqs. (36) and (37) respectively.

$$W = \int_0^{L_p \ \cos\ \varphi} p^*\, dx \tag{36}$$

$$\mu = \frac{1}{W}\int_0^{L_p \ \cos\ \varphi} \tau\, dx \tag{37}$$

4. Results and discussion

Results presented and discussed here are divided into three subsections. The first describes the numerical accuracy of the two scale method, the second subsection analyses the small scale simulations, and the third analyses contains results relating to smooth and textured surfaces at the large scale.

4.1. Numerical accuracy

Assessment of the numerical accuracy for the two-scale method is determined through grid independence of simulations at both scales and validation of the RSM used to couple these scales.

4.1.1. Grid independence

Small Scale grid independence was determined by varying the total number of elements for a specific case and comparing the mass flow rate produced. The absolute percentage error in mass flow rate against the mass flow rate with the largest number of nodes (25,000) is plotted in Fig. 5 for a topography amplitude $\alpha = 7.5\ \mu\text{m}$. In this simulation compressibility, piezoviscosity, and non-Newtonian (shear-thinning) behaviour were included, the cell pressure $p = 5$ MPa, the pressure gradient $dp/dx = -10$ MPa/mm, and the gap $g = 25\ \mu\text{m}$.

From Fig. 5 it was seen that the change in percentage error is reduced as the number of nodes increases illustrating convergence. 16,000 elements were chosen for this study. This allowed the small scale phenomena to be accurately captured at a moderate computational cost.

Grid independence at the large scale is considered by comparison of the mass flow rate predicted by the solver for a set case and geometry over a range of the number of nodes. Using the metamodel generated from small scale data where the topography amplitude $\alpha = 5\ \mu\text{m}$ and the flow phenomena are included the absolute percentage error in mass flow rate against the mass flow rate with the largest number of nodes (4000) was compared. The pad length, tilt angle, and load capacity were set to $L_p = 22.5$ mm, $\varphi = 0.05^\circ$, and $W = 100$ kN respectively and the result is shown in Fig. 6.

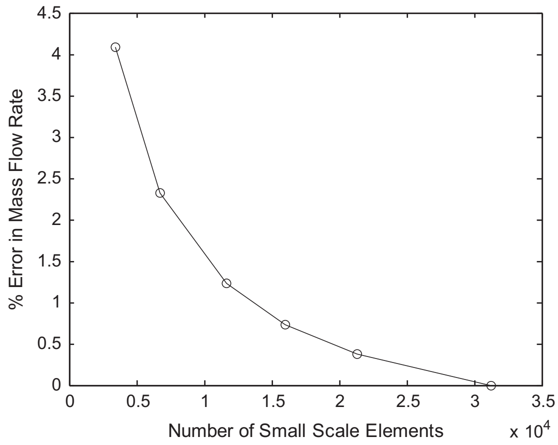

Fig. 5. Small scale grid independence.

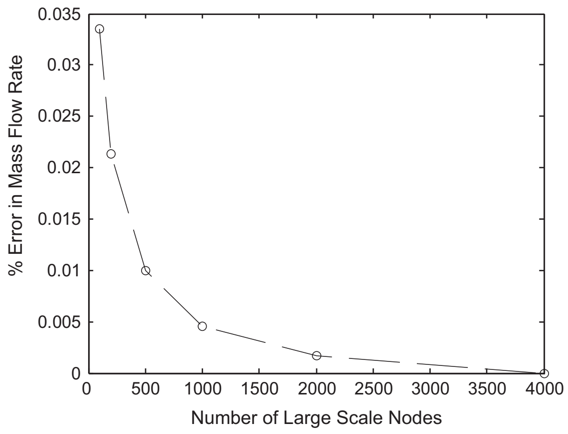

Fig. 6. Large scale grid independence.

Convergence is achieved as the error tends toward zero. For the purpose of this study a conservative 1000 nodes was chosen as an appropriate compromise between accuracy and computational expense.

4.1.2. RSM accuracy

The response surface approach used to couple the large and small scale simulations was validated through the accuracy of predicting Reynolds equation for incompressible, isoviscous flow against the smooth surface case and from homogenised small scale simulations where topography, compressibility, piezoviscosity, and non-Newtonian behaviour are present. To achieve this a 200 point DoE for each set of the small scale simulations was specified, populated, and the corresponding metamodels validated. These metamodels were then applied to a large scale simulation for which the load carrying capacity of the bearing was set to 100 kN, the pad length and tilt angle were $L_p = 22.5$ mm and $\varphi = 0.05^\circ$ respectively and the topography amplitudes investigated were $\alpha = 0$ and 7.5 μm.

From Figs. 7 and 8 it can be seen that the difference between the Reynolds and smooth surface pressure and film thickness solutions is negligible, demonstrating the accuracy of the multiscale method in modelling the smooth surface lubrication problem. In comparison to the smooth surface case it can be seen from Fig. 7 that due to the presence of topography and flow phenomena the maximum pressure reached in the bearing is lower and occurs closer toward the inlet. This has an impact on the distribution of deformation and as such the shape of the film

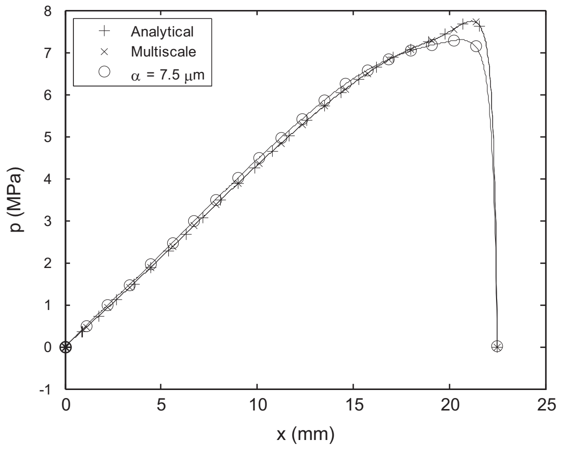

Fig. 7. Pressure distributions with and without topography.

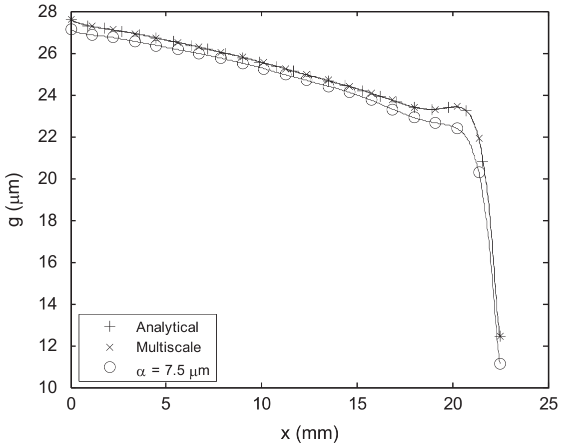

Fig. 8. Film thickness distributions with and without topography.

Table 3
Percentage error in mass flow rate inclusive of topography and flow phenomena.

Parameter	**Large scale *x*-coordinate**		
	0 mm	19.75 mm	22.5 mm
Pressure gradient, $\frac{dp}{dx}$ (MPa/mm)	0.4596	0	-31.74
Pressure, p (MPa)	0	7.297	0
Gap, g (μm)	27.14	22.08	11.14
% Error in mass flow rate	-0.2606	-0.0990	0.8334

thickness seen in Fig. 8. The film thickness is significantly decreased in magnitude across the length of the bearing.

In order to validate the trends presented in Figs. 7 and 8 results generated at the large scale through the metamodel are compared against the exact corresponding small scale simulations. The mass flow rate as predicted by the large scale solver is compared to the exact corresponding mass flow rate determined at the small scale for three locations along the distributions of pressure gradient, pressure and gap: maximum gap (0 mm), maximum pressure (19.75 mm), and minimum gap (22.5 mm). The results of this test are tabulated in Table 3.

The absolute percentage error in mass flow rate predicted between the metamodel and exact small scale simulations is $<1\%$ for all cases considered. This indicates that the metamodel is accurately capturing the effects of topography and flow phenomena upon bearing performance. This also validates the choice in size and spread of the DoE used.

4.2. Small scale solutions

Contours of small scale velocity components (u,v,w) from an example simulation are presented in Fig. 9 for two planes cut through the domain at $x=L/4$ and $x=3L/4$. In this simulation the cell pressure $p=5$ MPa, the pressure gradient $dp/dx=-20$ MPa/mm, the gap $g=10$ μm, and the topography amplitude $\alpha=7.5$ μm.

Fluid is driven through the domain by entrainment from the moving wall and the pressure jump leading to a majority of flow travelling in the x-coordinate direction. However in the presence of topography flow across the thickness of the film, cross-flow, and recirculation are observed. The patterns seen in these are non-symmetrical and can be attributed to the inclusion of inertial terms in the Navier–Stokes equations (Eq. (13)) used to govern flow at this scale.

Contours of pressure at the FSI interface and sliding wall are shown for this case in Figs. 10 and 11 respectively. Fig. 12 shows, for the same conditions, pressure contours in the film obtained from lubrication theory. The corresponding contours of film thickness for this example simulation are given in Fig. 13.

From Figs. 10 and 11 it is shown that pressure in the small scale domain is not constant through the film due to the presence of topography and use of the Navier–Stokes equations to describe fluid flow. This is in direct contrast to that predicted by lubrication theory at this scale under the same conditions (Fig. 12). The mass flow rate predicted by the Navier–Stokes solution was found to be 31.23% greater than that obtained from lubrication theory. The numerical cost of the Navier–Stokes solution was 193.0% of the lubrication solution. It is also shown in Figs. 10 and 11 that the jump in pressure over the domain which leads to the homogenised pressure gradient is not uniformly distributed. As such the cell pressure and load-per-unit-area at this scale differ and subsequently need to be defined separately. The distribution of film thickness shown in Fig. 13 is similar to that of the topography modelled such that as the solid spring column moves the shape of topography is maintained, although local deformation of topography does occur and is at least an order of magnitude or more smaller than average change in film thickness over the domain. The difference in film thickness between the upstream and downstream boundaries which leads to the near-periodic boundary condition for velocity is small but not negligible. With the result that the velocity field varies slowly from one cell to the next remaining consistent with the HMM used to derive the method.

4.3. Large scale solutions

In order to examine the tribological performance of the bearing, a range of pad lengths and tilt angles were specified and the resulting coefficients of friction and minimum film thicknesses examined under fixed load. With respect to the multiscale method developed and bearing performance two things are of particular interest: (i) the effect of compressibility, piezoviscosity, and non-Newtonian behaviour in conjunction with topography and (ii) the effect of the topography amplitude. Also analysed in this section is the micro-EHL effect of topography on the small scale minimum film thickness.

4.3.1. Effect of fluid flow phenomena

To examine the influence of flow phenomena on the tribological performance of the bearing three cases are considered: (i) incompressible, isoviscous, and Newtonian flow; (ii) inclusive of compressibility and piezoviscosity; (iii) with additional non-Newtonian (shear-thinning) behaviour to the phenomena

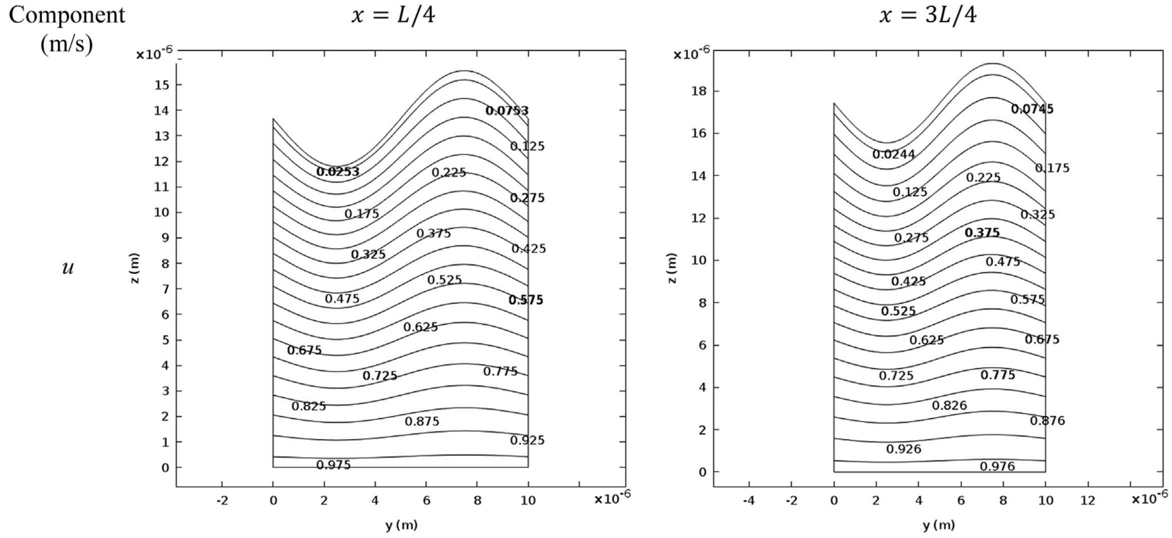

1a – u vs. y and z at x = L/4

2a - u vs. y and z at x = 3L/4

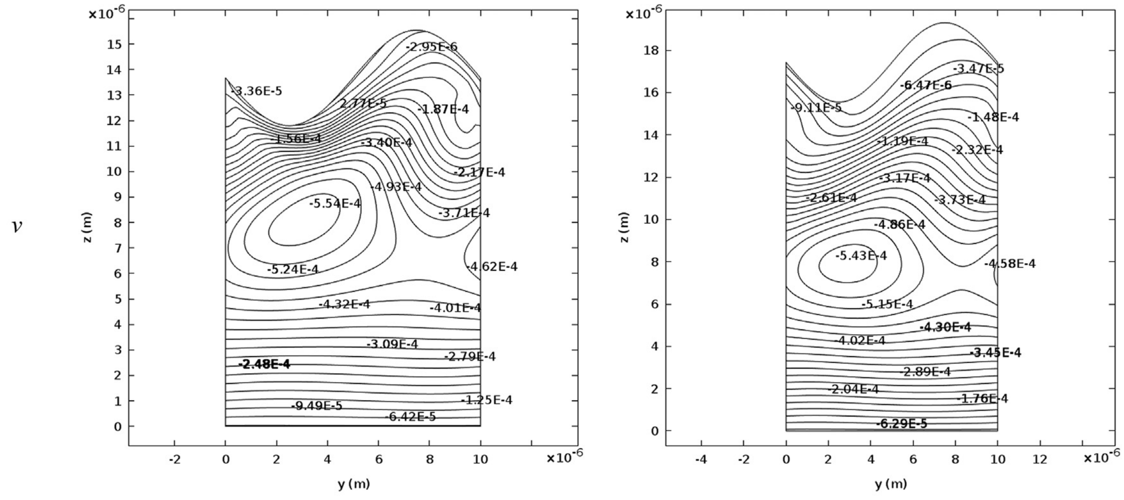

1b - v vs. y and z at x = L/4

2b - v vs. y and z at x = 3L/4

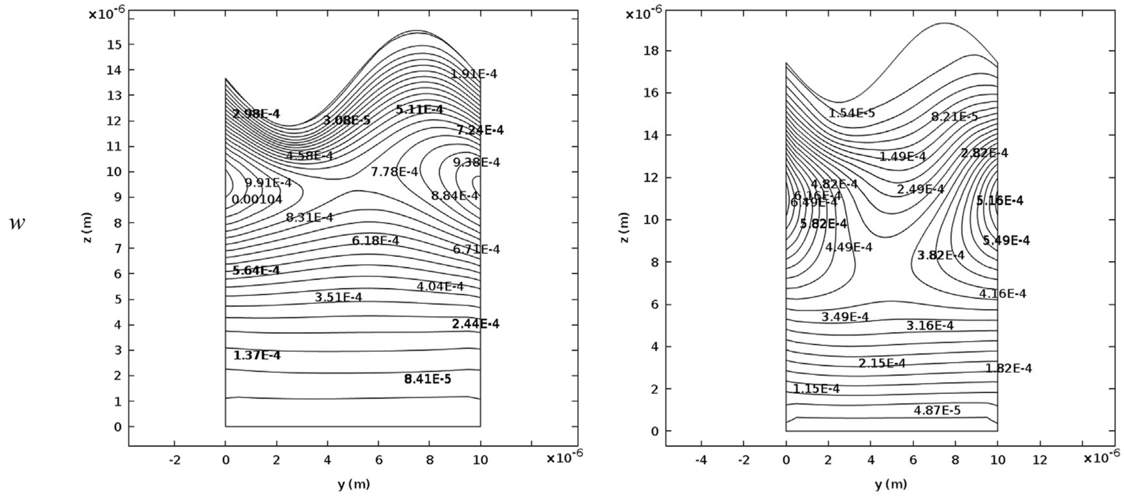

1c - w vs. y and z at x = L/4

2c - w vs. y and z at x = 3L/4

Fig. 9. Contours of small scale velocity components.

considered in (ii). The bearing load capacity was set $W=100$ kN, and the pad length and tilt angle were specified as $L_p=22.5$ mm and $\varphi=0.05^\circ$ respectively. The percentage difference in mass flow rate (q), coefficient of friction (μ), and minimum film thickness (g_b) produced from the two-scale method compared with lubrication theory are tabulated in Table 4.

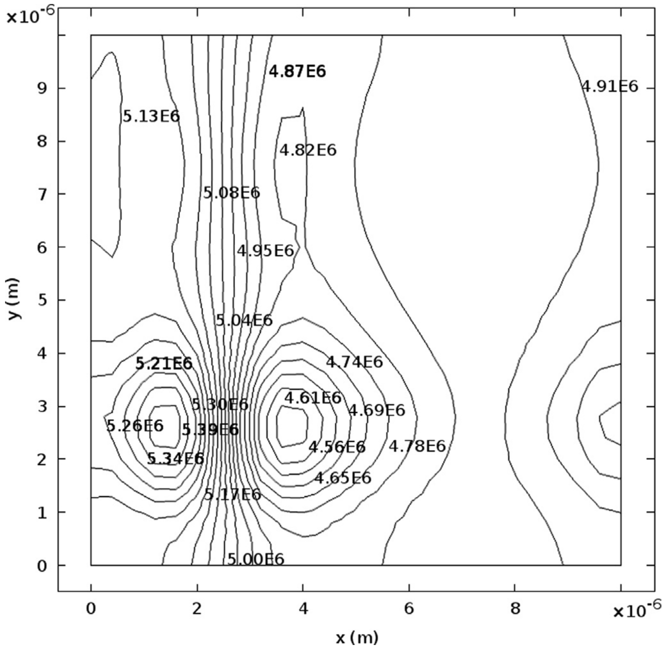

Fig. 10. Contours of pressure at the FSI interface.

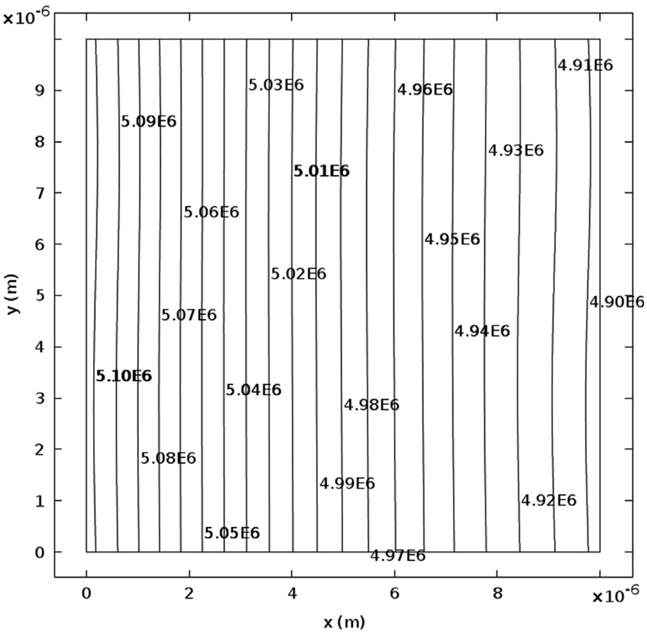

Fig. 11. Contours of pressure at the sliding wall.

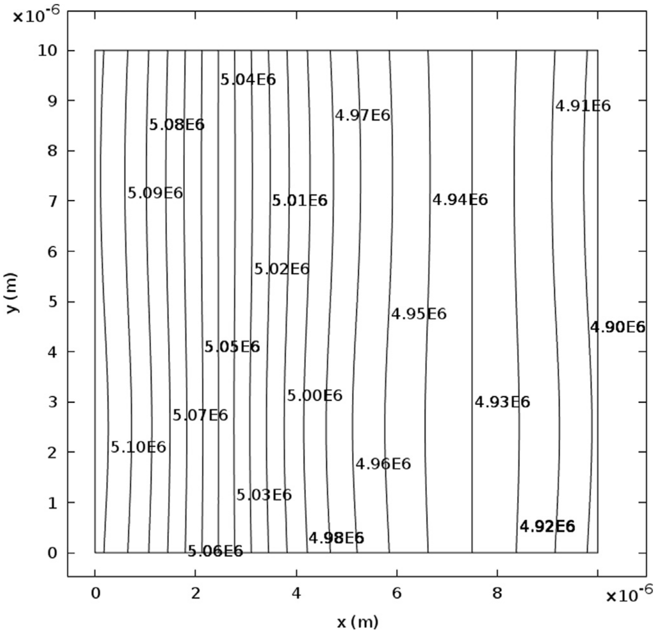

Fig. 12. Contours of pressure across the film obtained from lubrication theory.

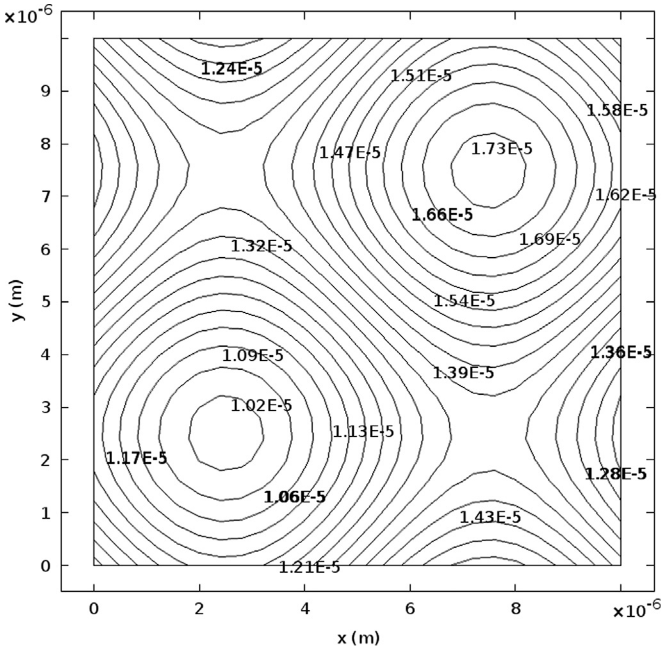

Fig. 13. Contours of film thickness.

Table 4
Percentage difference in bearing performance characteristics from the two-scale method with lubrication theory: Case (i) incompressible, isoviscous, $\alpha = 5\ \mu\text{m}$; Case (ii) compressible, piezoviscous; Case (iii) non-Newtonian (shear-thinning) behaviour.

Case	% Difference in q	% Difference in μ	% Difference in g_b
i	−7.44	8.23	−12.21
ii	−5.79	16.43	−9.99
iii	−5.79	16.44	−10.01

Table 4 shows that the two-scale method inclusive of topography predicts a lower mass flow rate and minimum film thickness than produced from lubrication theory, whereas the friction coefficient is increased. As compressibility and piezoviscosity are included in (ii) the magnitude of the mass flow rate, coefficient of friction, and minimum film thickness are, for a given pad length and tilt angle, increased from (i). The inclusion of non-Newtonian (shear-thinning) behaviour in (iii) has a negligible effect on the response when compared to (ii), where the mass flow rate, coefficient of friction, and minimum film thickness remain unchanged. Closer inspection of the small scale data used to generate Table 4 showed that the percentage difference in mass flow rate over all simulations between (i) and (ii) varied from −169.4 to 188.9%, and between (ii) and (iii) from −0.3 to 3.1%. Demonstrating that in combination with topography the effects of fluid flow phenomena should not be neglected. Much more significant effects due to these fluid flow phenomena would be experienced at higher pressures and shear rates than those modelled in this study. Overall, the non-linear influence of fluid flow phenomena on bearing performance has been successfully captured by the two-scale method and the metamodels representation of the small scale simulations.

4.3.2. *Effect of topography amplitude*

By incrementing the topography amplitude in steps of 2.5 μm from $\alpha = 0$ μm to 7.5 μm the change in performance of the bearing as the size of topography increases was investigated. For each value of the topography amplitude the small scale problem was solved and the metamodels constructed and validated. In order to illustrate the range of solutions possible from the metamodels created, parametric sweeps over pad length and tilt angle were performed for each load and topography amplitude investigated. Two loads were specified $W = 75$ kN and 100 kN, in the low load case the pad length $L_p \in [20, 22.5]$ mm and for the high load case $L_p \in [22.5, 25]$ mm. The tilt angle in both cases $\varphi \in [0.05, 0.06]^\circ$. The 75 kN result followed similar trends to the 100 kN result and are not included, the 100 kN result is presented in Fig. 14.

It is shown in Fig. 14 that increasing the topography amplitude tends to increase the magnitude of the coefficient of friction and reduce the magnitude of the minimum film thickness. Although

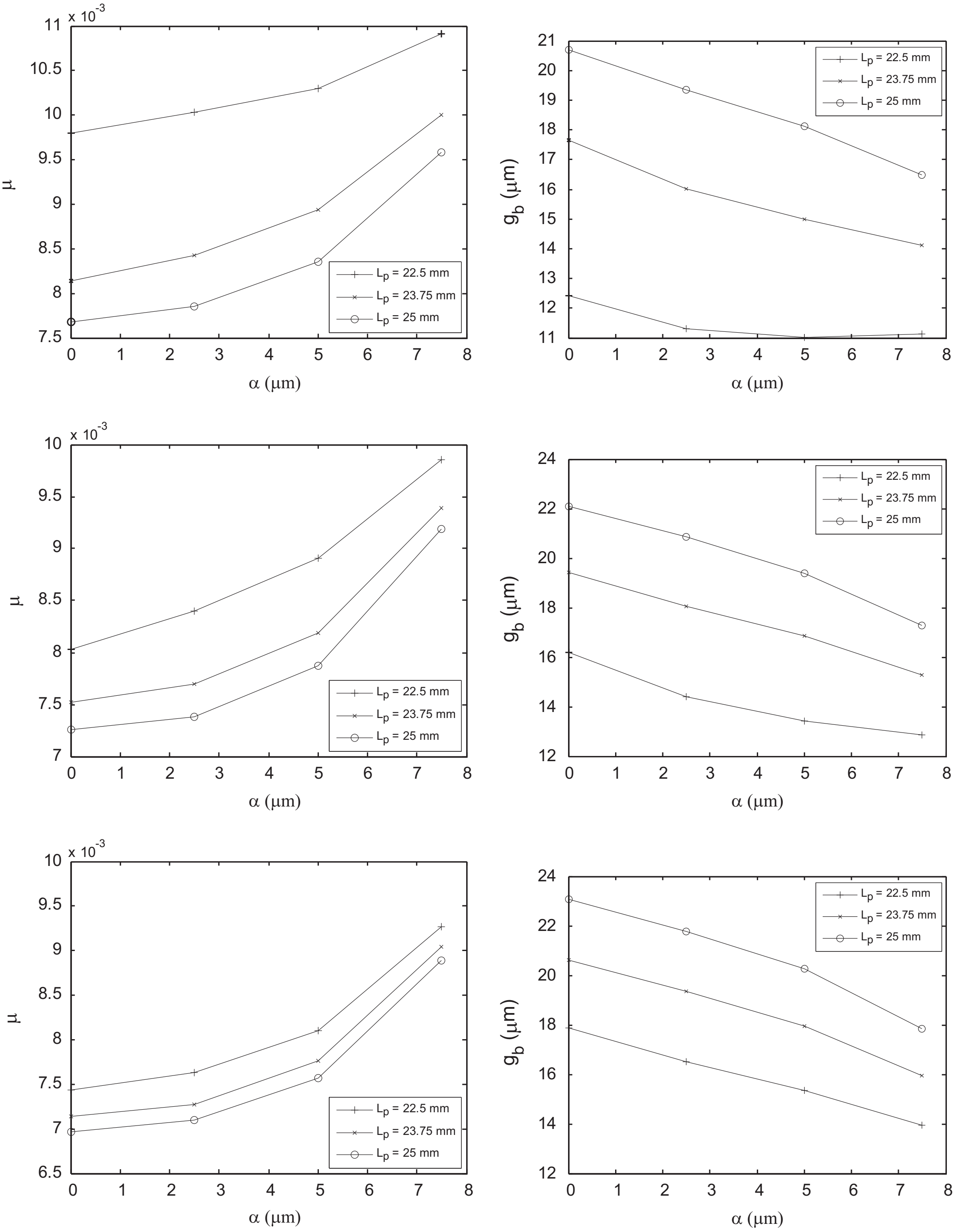

Fig. 14. Effect of topography amplitude on bearing performance.

for a topography amplitude of $\alpha=7.5\ \mu m$ the minimum film thickness remains almost constant for low values of pad length and tilt angle. For the topography amplitudes investigated, as both pad length and tilt angle are increased the coefficient of friction monotonically increases and the minimum film thickness monotonically decreases. It is also observed that as the topography amplitude is increased that the gradients of the responses with pad length and tilt angle are reduced, particularly in the region of low pad length and tilt angle. These large scale effects can be attributed to the flow features seen in the small scale simulations, where the presence of topography causes a change from lubrication theory in the pressure gradient – mass flow rate relationship derived.

4.3.3. *Micro-EHL effect on minimum film thickness*

To investigate the effect of micro-EHL on the minimum film thickness predicted by the two-scale method the parameter r is introduced.

$$r=\frac{s_{min}-(g+k_1 p)}{g+k_1 p}\times 100\% \tag{38}$$

Eq. (38) measures the percentage difference between the homogenised small scale minimum film thickness obtained with topography and the deformed film thickness predicted at the small scale without topography. r is therefore representative of the micro-EHL (separate from the large scale EHL) effect on film thickness in comparison to that which would be obtained from lubrication theory alone. Fig. A1 is a plot of r over the x-coordinate direction for a tilted-pad bearing of pad length $L_p=22.5$ mm, tilt angle $\varphi=0.05°$, load capacity $W=100$ kN and the topography amplitudes investigated are $\alpha=2.5\ \mu m$, $5\ \mu m$, and $7.5\ \mu m$.

The micro-EHL response on minimum film thickness in Fig. 15 illustrates a percentage difference in the range of -0.01 to -0.16% between that predicted by lubrication theory for a smooth surface and from the two-scale method inclusive of topography. This indicates that topography has deformed by an amount representative of the local stiffness and that the trends seen are due to the effects of flow phenomena and the presence of topography. The magnitude of r suggests that topography deforms locally by an amount at least an order of magnitude or more smaller than that representative of the local stiffness, coinciding with the evidence draw from Fig. 13. The minimum film thickness achieved at the small scale is less than that achieved from column deformation of a smooth surface. Increasing the topography amplitude generates with some deviation a larger magnitude of r. The relationship between r and the pressure, pressure gradient, and film thickness is complex with some dependency of the parameters observed. As the film thickness is decreased and pressure increased along the bearing length r is reduced. A peak in r exists at the location of maximum pressure. Toward the outlet of the bearing where there is a reduction in both pressure and film thickness there is also a corresponding drop in r.

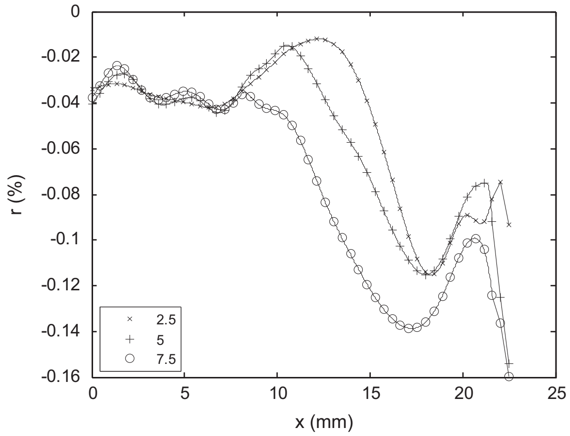

Fig. 15. Micro-EHL effect on minimum film thickness.

5. Conclusion

Based on the HMM a new two-scale method for EHL and micro-EHL analyses was developed and applied to tilted-pad bearings with three-dimensional topography. Elastic deformation together with the Navier–Stokes equations inclusive of compressibility, piezoviscosity, and non-Newtonian (shear-thinning) behaviour describe the small scale problem. A pressure gradient – mass flow rate relationship was used to couple the two scales. By decomposing the stiffness matrix into diagonal and non-diagonal terms elastic deformation of the bearing surface was addressed at both the large and small scales. An inverse spring method was introduced in order to model any stiffness at the large scale whilst maintaining assumptions of the multiscale theory at the small scale. Small scale solutions were homogenised and through interpolation used at the large scale. A MLS metamodel was used to represent the small scale solutions as a root to interpolation, this process of metamodel building was validated using k-fold CV.

Grid independence and metamodel validation showed that the small scale effects were accurately captured and described at the large scale. Results using this method agreed well with lubrication theory in the smooth surface case. Contours of small scale velocity components illustrated that non-symmetrical fluid flow patterns not described by lubrication theory occur in the presence of topography and that homogenisation of the small scale problem captures micro-EHL effects not described at the large scale. Analysis at the large scale showed that compressibility and piezoviscosity had a far more significant effect on bearing performance than non-Newtonian behaviour, although more significant effects would be observed at higher pressures than those modelled. For a given pad length and tilt angle it was shown at constant load that the inclusion of topography produced a lower maximum pressure which was located closer toward inlet and the film thickness was reduced. Increasing topography amplitude at constant load over a range of pad lengths and tilt angles lead to an increase in the friction coefficient and reduction in minimum film thickness. Also the gradients at which both responses increased with pad length and tilt angle were reduced. The micro-EHL effect on minimum film thickness was quantified and shown to be at least an order of magnitude smaller than that representing local stiffness.

The aim of this study was to include three-dimensional topography and representative lubricant behaviour at the small scale into a tilted-pad bearing at the large scale. Expanding the study to include cavitation at both scales would allow analysis of converging–diverging geometries such as those found in line and point contacts. The higher pressures generated in such simulations could be modelled so long as the assumption surrounding the difference in scales between the size (and deformation) of topography and the equivalent thickness is maintained. Parameterisation of topography as discussed in Section 2.3.2 would, at some numerical expense, elucidate the general solution over the range of parameters investigated and potentially allow quantitative comparison with existing tools for waviness in EHL contacts. Where the large scale problem has cross-flow or side-leakage, pressure gradients parallel to the direction of flow could be implemented. For simulations of this manner the large scale solver would need to account for the mass flow rates in both directions as well as the partial differential equation coupling both pressure gradients. Each pressure gradient would require four terms which define the small scale simulations: a characteristic gap, pressure, and mass flow rates in both directions. A significant increase in complexity and numerical cost for the general large scale case therefore exists. Further investigation into how the two-scale method is affected by temporal discretisation is required before any definitive general method for transient flow can be described.

Acknowledgements

The authors would like to thank the School of Mechanical Engineering, Univeristy of Leeds for their support throughout this project and the Engineering and Physical Sciences Research Council (Grant number EP/I013733/1) for funding some of this work.

Appendix A

Note that the two-scale method does not form an iterative cycle. The system shown highlights the important equations at each scale and the flow of information from one component to the next. The dotted lines indicate that all required information is passed as a prerequisite to the next stage, whereas the solid line shows where information is passed during the solution process (Fig. A1).

Referees

Guillermo Morales-Espejel, SKF Engineering and Research Centre, Kelvinbaan 16, 3430 DT, Nieuwegein, The Netherlands. Email: guillermo.morales@skf.com

Andreas Almqvist, Department of Engineering Sciences and Mathematics, Lulea University of Technology, Universitetsområdet, Porsön, 971 87 Lulea, Sweden. Email: Andreas.Almqvist@ltu.se

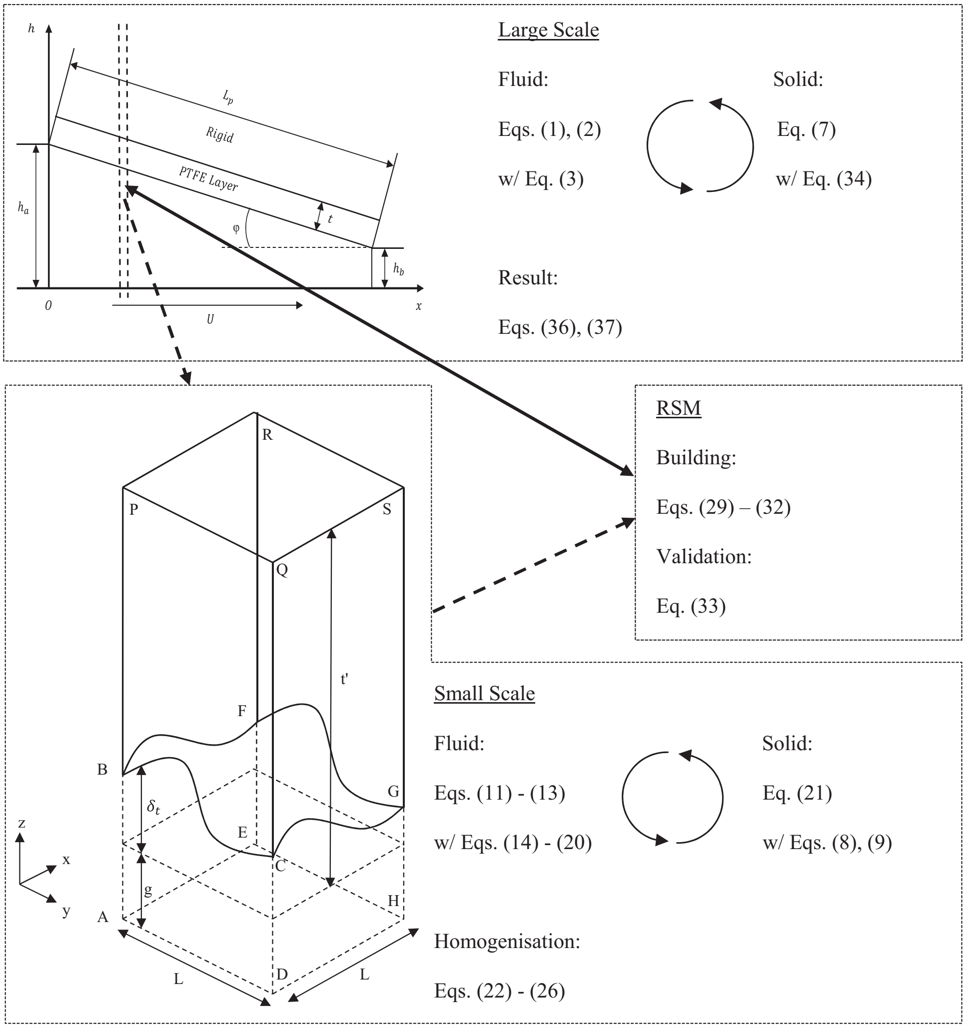

Fig. A1. Graphical summary of the two-scale method.

Ron van Ostayen, Department of Precision and Microsystems Engineering, Delft University of Technology, Mekelweg 2, 2628 CD DELFT, The Netherlands. Email: R.A.J.vanOstayen@tudelft.nl

References

[1] Reynolds O. On the theory of lubrication and its application to Mr. Beauchamp Tower's experiment, including an experimental determination of the viscosity of olive oil. Philos Trans Royal Soc Lond 1886;177:157–234.

[2] Dowson D, Higginson GR. A numerical solution to the elasto-hydrodynamic problem. Proc Inst Mech Eng-Part C: J Mech Eng Sci 1959;1:6.

[3] Tzeng ST, Saibel E. Surface roughness effect on slider bearing lubrication. ASLE Trans 1967;10:334–8.

[4] Etsion I, Kligerman Y, Halperin G. Analytical and experimental investigation of laser-textured mechanical seal faces. Tribol Trans 1999;42:511–6.

[5] Venner CH, Lubrecht AA. Amplitude reduction of non-isotropic harmonic patterns in circular EHL contacts, under pure rolling. In: Dowson D, et al., editors. Lubrication at the frontier. Proceedings of the 25th leeds-lyon symposium on tribology, vol. 34, The Netherlands: Elsevier; 1999. p. 151–62.

[6] Morales-Espejel GE, Lugt PM, van Kuilenburg J, Tripp JH. Effects of surface micro-geometry on the pressures and internal stresses of pure rolling EHL contacts. Tribol Trans 2003;46:260–72.

[7] Hooke CJ, Li YK, Morales-Espejel GE. Rapid calculation of the pressures and clearances in rolling-sliding elastohydrodynamically lubricated contacts, Part 2: general non-sinusoidal roughness. Proc Inst Mech Eng-Part C: J Mech Eng Sci 2007;221:555–64.

[8] Krupka I, Hartl M. The effect of surface texturing on thin EHD lubrication films. Tribol Int 2007;40:1100–10.

[9] Szeri AZ. Fluid film lubrication: theory and design. Cambridge, UK: Cambridge University Press; 1998.

[10] van Odyck D, Venner C. Stokes flow in thin films. J Tribol 2003;125:121–34.

[11] Tichy J, Bou-Said B. On the transition from reynolds to stokes roughness. In: Lubrecht, Dalmaz, editors. Transient process in tribology, 43. The Netherlands: Elsevier; 2003. p. 235–42.

[12] Arghir M, Roucou N, Helene M, Frene J. Theoretical analysis of the incompressible laminar flow in a macro-roughness cell. J Tribol 2003;125:309–18.

[13] Sahlin F, Glavatskih S, Almqvist T, Larsson R. Two-dimensional CFD-analysis of micro-patterned surfaces in hydrodynamic lubrication. J Tribol 2005;127:96–102.

[14] Dobrica M, Fillon M. About the validity of reynolds equation and inertia effects in textured sliders with infinite width. Proc Inst Mech Eng-Part J: J Eng Tribol 2009;223:69–78.

[15] Cupillard S, Glavatskih S, Cervantes M. Inertia effects in textured hydrodynamic contacts. Proc Inst Mech Eng-Part J: J Eng Tribol 2010;224:751–6.

[16] Gao L, Hewson RW. A multiscale framework for EHL and micro-EHL. Tribol Trans 2012;55:713–22.

[17] Wilson S, Duffy B. On lubrication with comparable viscous and inertia forces. Q J Mech Appl Math 1998;51:105–24.

[18] Hartinger M, Dumont M-L, Ioannides S, Gosman D, Spikes H. CFD modelling of thermal and shear-thinning elastohydrodynamic line contact. J Tribol 2008;130:014503.

[19] Aurelian F, Patrick M, Mohamed H. Wall slip effects in (Elasto) hydrodynamic journal bearings. Tribol Int 2011;44:868–77.

[20] Bruyere V, Fillot N, Morales-Espejel GE, Vergne P. Computational fluid dynamics and full elasticity model for sliding line thermal elastohydrodynamic contacts. Tribol Int 2011;46:3–13.

[21] Mourier L, Mazuyer D, Ninove F-P, Lubrecht A. Lubrication mechanisms with laser-textured surfaces in the elastohydrodynamic regime. Proc Inst Mech Eng-Part J: J Eng Tribol 2010;224:697–712.

[22] Zhu D, Nanbu T, Ren N, Yasuda Y, Wang Q. Model-based virtual surface texturing for concentrated conformal-contact lubrication. Proc Inst Mech Eng-Part J: J Eng Tribol 2010;224:685–96.

[23] Gao L, Yang P, Dymond I, Fisher J, Jin Z. Effect of surface texturing on the elastohydrodynamic lubrication analysis of metal-on-metal hip implants. Tribol Int 2010;43:1851–60.

[24] Félix-Quiñonez A, Ehret P, Summers JL. On three-dimensional flat-top defects passing through an ehl point contact: a comparison of modelling with experiments. J Tribol 2005;127:51–60.

[25] Jai M, Bou-Said B. A comparison of homogenization and averaging techniques for the treatment of roughness in slip-flow-modified reynolds equation. J Tribol 2002;124:327–35.

[26] Sahlin F, Almqvist A, Larsson R, Glavatskih S. Rough surface flow factors in full film lubrication based on a homogenization technique. Tribol Int 2007;40:1025–34.

[27] Sahlin F, Larsson R, Almqvist A, Luft P, Marklund P. A mixed lubrication model incorporating measured surface topography. Part 1: theory of flow factors. Proc Inst Mech Eng-Part J: J Eng Tribol 2010;224:335–51.

[28] Martin S. Influence of multiscale roughness patterns in cavitated flows: application to journal bearings. Math Probl Eng 2008;2008:439319.

[29] Li J, Chen H. Evaluation on applicability of reynolds equation for squared transverse roughness compared to CFD. J Tribol 2007;129:963–7.

[30] Patir N, Cheng H. An average flow model for determining effects of three-dimensional roughness on partial hydrodynamic lubrication. J Tribol 1978;100:12–7.

[31] de Kraker A, van Ostayen R, Beek A, Rixen D. A multiscale method for modelling surface texture effects. J Tribol 2007;129:221–30.

[32] de Kraker A, van Ostayen RAJ, Rixen DJ. Development of a texture averaged reynolds equation. Tribol Int 2010;43:2100–9.

[33] Hewson R, Kapur N, Gaskell P. A two-scale model for discrete cell gravure roll coating. Chem Eng Sci 2011;66:3666–74.

[34] E. W, Engquist B. The heterogeneous multi-scale methods. Commun Math Sci 2003;1:87–133.

[35] Loweth EL, de Boer GN, Toropov VV. Practical recommendations on the use of moving least squares metamodel building. In: Topping BHV, Tsompanakis Y, editors. Proceedings of the 13th international conference on civil, structural and environmental engineering computing, vol. 96, Stirlingshire: Civil-Comp Press; 2011.

[36] Narayanan A, Toropov VV, Wood A, Campean IF. Simultaneous model building and validation with uniform designs of experiments. Eng Optim 2007;39:497–512.

[37] Bates SJ, Sienz J, Toropov, VV. , Formulation of the optimal latin hypercube designs of experiments using a permutation genetic algorithm. In: Proceedings of the 45th AIAA/ASME/ASCE/AHS/ASC structures, structural dynamics & materials conference; 2004.

[38] Toropov VV, Bates S, Querin OM. Generation of uniform latin hypercube designs of experiments. In: Topping BHV, editors. Proceedings of the 9th international conference on the application of artificial intelligence to civil, structural and environmental engineering, vol. 7; 2007.

[39] Cameron A. Basic lubrication theory. London: Longman; 1971.

[40] Sadd MH. Elasticity—theory, applications, and numerics. Amsterdam: Elsevier; 2009.

[41] Ferziger JH, Perić M. Computational methods for fluid mechanics. London: Springer; 2002.

[42] Dowson D, Higginson GR. Elastohydrodynamic lubrication: the fundamentals of roller and gear lubrication. Oxford: Pergamon; 1966.

[43] Roelands C. Correlational aspects of the viscosity-temperature-pressure relationship of lubricating oils [Ph.D. thesis]. Delft: Technical University Delft; 1966.

[44] Bair S, Kottke P. Pressure–viscosity relationships for elastohydrodynamics. Tribol Trans 2003;46(3):289–95.

[45] Johnson KL, Tevaarwerk JL. The shear behaviour of elastohydrodynamic oil films. Proc Royal Soc Lond, Ser A 1977;356:215–36.

[46] Bair S, Jarzynski J, Winer WO. The temperature, pressure and time dependence of lubricant viscosity. Tribol Int 2001;34:461–86.

[47] Benham PP, Crawford RJ, Armstrong CG. Mechanics of engineering materials. 2nd ed.. London: Pearson; 1996.

[48] Box GEP, Draper NR. Response surfaces, mixtures and ridge analyses. 2nd ed.. New York: Wiley and Sons; 2007.

[49] Keane AJ, Nair PB. Computational approaches for aerospace design: the pursuit of excellence. New York: Wiley and Sons; 2005.

[50] Forrester A, Sóbester A, Keane A. Engineering design via surrogate modelling: a practical guide. New York: Wiley and Sons; 2008.

[51] Myers RH, Montgomery DC, Anderson-Cook CM. Response surface methodology: process and product optimization using designed experiments. 3rd ed.. New York: Wiley and Sons; 2009.

[52] Rodkiewicz C, Yang P. Proposed TEHL solution system for the trust bearings inclusive of surface deformations. Tribol Trans 1995;38:75–85.